

MRI of Blood Flow of the Human Retina

Qi Peng,^{1,2} Yi Zhang,^{1,2} Oscar San Emeterio Nateras,² Matthias J.P. van Osch,³
and Timothy Q. Duong^{1,2,4–6*}

This study reports a high-resolution MRI approach to image basal blood flow and hypercapnia-induced blood-flow changes in the unanesthetized human retina on a 3-T MRI scanner. Pseudo-continuous arterial spin labeling technique with static tissue suppression was implemented to minimize movement artifacts and improve blood-flow sensitivity. Turbo spin-echo acquisition was used to achieve high spatial resolution free of susceptibility artifacts. The size, shape, and position of a custom-made receive radiofrequency coil were optimized for sensitivity in the posterior retina. Synchronized eye blink and respiration to the end of each data readout minimized eye movement and physiological fluctuation. Robust high-contrast blood-flow MRI of the unanesthetized human retina was obtained at $500 \times 800 \mu\text{m}^2$ in-plane resolution. Blood flow in the posterior retina was $93 \pm 31 \text{ mL}/(100 \text{ mL min})$ (mean \pm standard deviation, $N = 5$). Hypercapnic inhalation (5% CO_2) increased blood flow by $12 \pm 4\%$ relative to air ($P < 0.01$, $N = 5$). This study demonstrates the feasibility of blood-flow MRI of the retina of unanesthetized human. Because blood flow is tightly coupled to metabolic function under normal conditions and it is often perturbed in diseases, this approach could provide unique insights into retinal physiology and serve as an objective imaging biomarker for disease staging and testing of novel therapeutic strategies. This approach could open up new avenue of retinal research. Magn Reson Med 65:1768–1775, 2011. ©2011 Wiley-Liss, Inc.

Key words: ASL; retinal vessels; choroids; high-resolution MRI; hypercapnia

Blood flow (BF) in the brain is intricately coupled to basal metabolic function under normal physiological conditions, and it is often perturbed in disease states (1). Basal BF and its responses to stimulations have been used as imaging biomarkers for early detection,

disease staging, and longitudinal monitoring of therapeutic intervention in the brain. Similar studies probing BF and neurovascular coupling in the retina are sparse by comparison, in part due to the lack of sufficiently high spatial resolution and quantitative BF imaging techniques for the retina in vivo. Abnormal basal BF and neurovascular coupling to stimulations may play an important role in many retinal diseases, including glaucoma and diabetic retinopathy, and retinal ischemia (see Refs. 2,3).

In vivo BF imaging of the retina has been reported using fluorescein angiography (4), indocyanin-green angiography (5), laser Doppler flowmetry (LDF) (6), and laser speckle imaging (7,8). While these BF techniques have made remarkable contributions to our understanding of normal retinal physiology and pathophysiology, they are qualitative and depth ambiguous. Choroidal vessels are behind the usually opaque retinal pigment epithelium. Moreover, optical scattering and disease-induced opacity, such as vitreal hemorrhage and cataract, could hamper efficacy of optical imaging techniques.

MRI, by contrast, provides quantitative BF images of the brain without depth limitation, and BF MRI has been used for studying brain physiology and pathophysiology. BF can be measured quantitatively by dynamic susceptibility contrast MRI using an exogenous contrast agent (9) or by magnetically labeling the endogenous water in blood using the arterial spin labeling (ASL) technique (10–12). The dynamic susceptibility contrast MRI technique is efficient but it is incompatible with time-series BF functional MRI and high-resolution BF MRI because the long half-life of the contrast agent allows only one measurement per bolus injection, precluding time-series measurement and signal averaging to augment signal-to-noise ratio (SNR). The ASL technique, on the other hand, is totally noninvasive, and the labeled water has a favorable short half-life (blood water T_1 of $\sim 1 \text{ sec}$), ideally suited for time series and high-resolution BF MRI. Quantitative BF MRI also allows comparison across experimental groups.

High-resolution BF MRI of normal retina (13) and retinal degeneration (14) in anesthetized rodents has been reported recently. BF MRI of the human retina is however more challenging because: (i) magnetic field gradients on clinical scanners are weaker than animal scanners, making it difficult to achieve high spatial resolution to image the thin retina, (ii) the eye is located in a region of large magnetic field inhomogeneity and is thus susceptible to signal drop off and image distortion when a typical echo-planar imaging technique is used for fMRI studies, and (iii) eye motion in awake humans could constitute an additional challenge for BF MRI, which requires pairwise subtraction. With the exception of a

¹Research Imaging Institute, University of Texas Health Science Center, San Antonio, Texas, USA.

²Department of Radiology, University of Texas Health Science Center, San Antonio, Texas, USA.

³Department of Radiology, Leiden University Medical Center, C.J. Gorter Center for High Field MRI, Leiden, The Netherlands.

⁴Department of Ophthalmology, University of Texas Health Science Center, San Antonio, Texas, USA.

⁵Department of Physiology, University of Texas Health Science Center, San Antonio, Texas, USA.

⁶South Texas Veterans Health Care System, San Antonio, Texas, USA.

Grant sponsors: Clinical Translational Science Award Pilot Grant, Translational Technology Resource Grant to TQD (Parent; Grant number: UL1RR025767); Grant sponsor: NIH/NEI; Grant numbers: R01 EY014211, EY018855 to TQD; Grant sponsor: Department of Veterans Affairs (VISN7 Career Development Award and MERIT to TQD).

*Correspondence to: Timothy Q. Duong, Ph.D., Research Imaging Institute, University of Texas Health Science Center at San Antonio, 8403 Floyd Curl Drive, San Antonio, Texas 78229. E-mail: duongt@uthscsa.edu

Received 25 August 2010; revised 25 October 2010; accepted 24 November 2010.

DOI 10.1002/mrm.22763

Published online 24 February 2011 in Wiley Online Library (wileyonlinelibrary.com).

© 2011 Wiley-Liss, Inc.

conference abstract using a head-volume coil (15), there are no reports of BF MRI studies of the human retina to our knowledge.

The goals of this study were to explore the feasibility of imaging basal BF and BF responses to hypercapnic inhalation in the unanesthetized human retina using MRI. A custom-made receive-only eye coil was used to improve SNR on a 3-T clinical MRI scanner. Pseudocontinuous arterial spin-labeling technique (16) with background suppression and single-shot turbo spin-echo (TSE) acquisition were implemented. pCASL was used to improve BF sensitivity, background suppression was used to enhance sensitivity and minimize eye movement artifacts, and TSE was used to achieve high spatial resolution free of susceptibility-induced signal drop off and image distortion. Strategies (such as synchronized eye blink and inhalation) to minimize eye motion were implemented. Quantitative basal BF and hypercapnia-induced BF changes were analyzed.

MATERIALS AND METHODS

Subject Preparations

Five healthy subjects (4 males, 1 female, 24–45 years old) were studied with Institutional Review Board approval. Each subject was imaged in multiple sessions on different days. Multiple trials (scan with each trial lasting 8 min) were acquired within each session. Subjects were instructed to maintain stable eye fixation on a target inside the magnet bore with synchronized eye blink to the end of data readout which generated a distinct sound as a cue. Subjects were also instructed to synchronize inhalation (or exhalation) only to the end of the data readout throughout the entire trial. With an inter-image repetition time of 4.6 sec, such synchronized breathing and blinking were within comfort.

Basal BF measurements during air inhalation were acquired over 8 min. For gas challenge, serial BF MRI was acquired during 4 min air followed by 4 min hypercapnia (5% CO₂, 21% O₂ and balance N₂). Premixed gas was delivered via an inhalation face mask. The total scan duration for each trial was 8 min. A break of 5–10 min was given between trials.

MRI

MRI was performed on a 3 T Phillips whole-body clinical scanner (Achieva, Philips Healthcare, Best, The Netherlands) using the commercial body radiofrequency (RF) coil for transmission and a custom-built single-loop RF coil mounted on a pair of swimming goggles for reception (oval shape, 7 × 5 cm² in diameter, right eye only). To demonstrate feasibility and to minimize partial-volume effect (PVE), only a single central axial slice bisecting the optic nerve head and fovea of the right eye was imaged.

BF was imaged using the pCASL technique with: RF pulse shape = Hanning window, RF pulse duration = 0.5 msec, flip angle = 18°, interpulse pause = 0.5 msec, maximum labeling gradient = 6 mT/m, labeling duration = 2 sec, and postlabeling delay = 1.5 sec with balanced gradient scheme. The control images were acquired with

a 180° phase shift to the labeling RF pulse. The ASL labeling plane was 7 cm inferior to the imaging plane. ASL background suppression employed two inversion pulses at 2061 and 3405 msec after the initial saturation pulse, which was placed before the labeling pulse (17). These two inversion times were optimized based on simulations (Matlab algorithms) to minimize vitreous and retinal signal using the experimental parameters and assuming vitreous $T_1 = 4163$ msec and retina $T_1 = 1015$ msec which were assumed to be similar to those of the cerebrospinal fluid and gray matter at 3.0 T, respectively. These inversion delays were experimentally fine-tuned and confirmed to achieve necessary vitreous suppression and static tissue signal suppression.

Image acquisition used the single-shot TSE sequence with: pulse repetition time = 4.6 sec, echo time = 30 msec, slice thickness = 6 mm, bandwidth = 12.8 kHz, TSE factor = 28, field of view = 50 × 43 mm, and matrix = 100 × 53 (resolution of 500 × 800 μm²). The higher spatial resolution was placed along the readout direction, perpendicular to the posterior retina. Half-Fourier acquisition (52.5%) and linear profile ordering were used along the phase-encode direction, leading to a total TSE echo train length of 343 msec. Spatial-selective gradients were applied along with RF refocusing pulses to avoid aliasing artifacts along the phase-encode direction (18). Label and control images were acquired alternately with a temporal resolution of 9.2 sec per paired image. A separate TSE scan without labeling module and inversion pulses with long pulse repetition time = 15 sec was performed to obtain M_0 for BF calculation. This protocol showed no residual magnetization-transfer effect when the labeling plane was shifted to 7 cm superior to the imaging plane. Finally, the first refocusing pulse was 180° and the rest of the refocusing pulses were 160°. Due to the small field of view along the phase encode direction, only 28 refocusing pulses were applied during each pulse repetition time cycle. Based on the safety monitor of the scanner, the SAR was 2.9 W/kg when pulse repetition time = 4.6 sec, which was below the FDA-recommended limit.

Data Analysis

All images from each trial were first aligned using custom algorithms written in Matlab (MathWorks Inc., Natick, MA). Image intensity profiles across the retinal thickness were automatically drawn from the raw ASL images by radially projecting lines perpendicular to the retina (19) with eight times spatial interpolation. Some interpolations were necessary for the profile analysis to be completely automated and such spatial interpolation was previously confirmed not to significantly alter peak width and height (19). Profiles at different time points were then coregistered to the averaged profile by minimizing the root mean square distances. Outlier images due to severe motion artifacts induced by unintended blinking during data readout were discarded (about 4% of the time-series images). Aligned images were played in bounced movie to ensure no residual motion or drift before further processing.

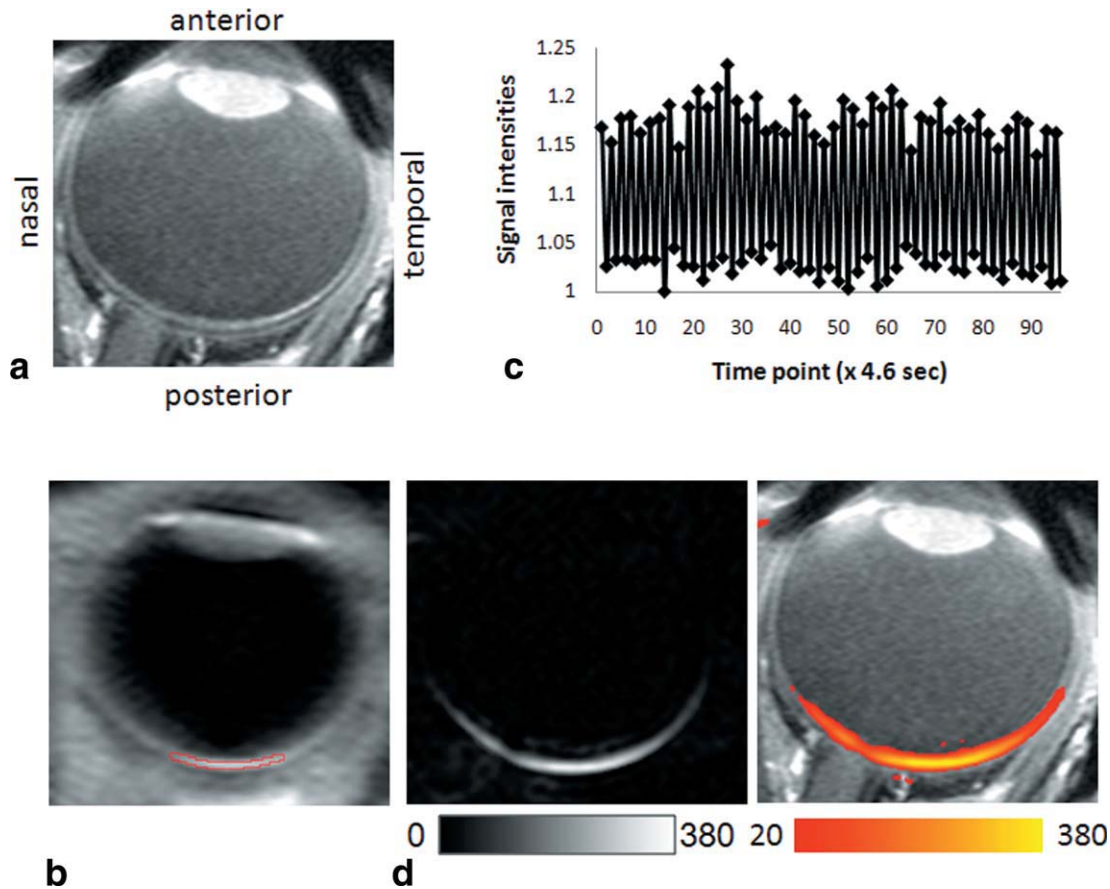


FIG. 1. (A) T_1 -weighted scout image demonstrating the anatomical structure. (B) Representative control image from the pCASL scan with the ROI overlaid on the retina. (C) Time course of the control and label images from the ROI of the posterior retina as shown in (B). (D) Quantitative blood flow under basal condition in gray and color scale overlaid on a T_1 -weighted scout image. Scale bars indicate units of mL/(100 mL min). [Color figure can be viewed in the online issue, which is available at wileyonlinelibrary.com.]

Voxel-by-voxel BF were quantified in units of mL/(100 mL min) to generate the BF map based on (20):

$$BF = \frac{6000}{2 \cdot \lambda \cdot \alpha \cdot \alpha_{inv} \cdot T_{1,blood}} \cdot \frac{\Delta M_{ASL}}{M_0} \cdot e^{TI/T_{1,blood}} \cdot e^{TE/T_{2,blood}}$$

where ΔM_{ASL} is the difference of the control and label images. λ is the milliliter water per milliliter arterial blood (0.85) (21), blood $T_{1,blood}$ and $T_{2,blood}$ are 1.7 sec at 37°C (22) and 275 msec at 3 T (23). α , the arterial spin-labeling efficiency, was assumed to be 0.85 (24). α_{inv} was 0.83 which corrected for the loss of perfusion signal due to the two background suppression pulses (25), inversion time is the post-labeling delay and M_0 is the equilibrium signal intensity of vitreous calculated from the reference scan. The equilibrium signal intensity of vitreous was used as an intensity reference for pure water, avoiding the use of unknown retina-blood partition coefficient in the quantitative BF calculation.

Cross-correlation Z-score “activation” maps for display purpose were calculated via FSL software (26) by matching the BF signal time courses to the expected stimulus paradigm. Color statistical maps were overlaid on BF images. To objectively quantify BF data and minimize PVE-automated profile, analysis was performed to generate the BF profiles across the thickness of the retina and along the length of the retina (19). BF values for the

entire retinal thickness were determined as a function of the distance from the optic nerve head, where the BF values were taken at the peaks of the projection profiles. A region of interest (ROI) of the posterior retina was used to obtain the BF signal time courses and averaged BF values during air or hypercapnic inhalation. Data during transition (1 min) from air to hypercapnic inhalation was excluded from percent-change calculation.

All reported values and error bars on graphs were in mean \pm standard deviation. All statistical tests employed one-way ANOVA with correction for correlated samples with a $P < 0.05$ indicating statistical significance unless otherwise stated.

RESULTS

The size and curvature of a custom-built receive-only RF coil were carefully optimized to achieve the highest SNR at the posterior retina. The RF coil was mounted onto a custom-made swimming eye goggle, providing comfort, stability, and consistency. Retinal MRI free of movement artifacts was obtained by employed fixation strategy described above. Infrequent, minor movement and drift were successfully corrected with image coregistration.

Figure 1 shows an anatomical image, a representative pCASL control image, a time course of control and label

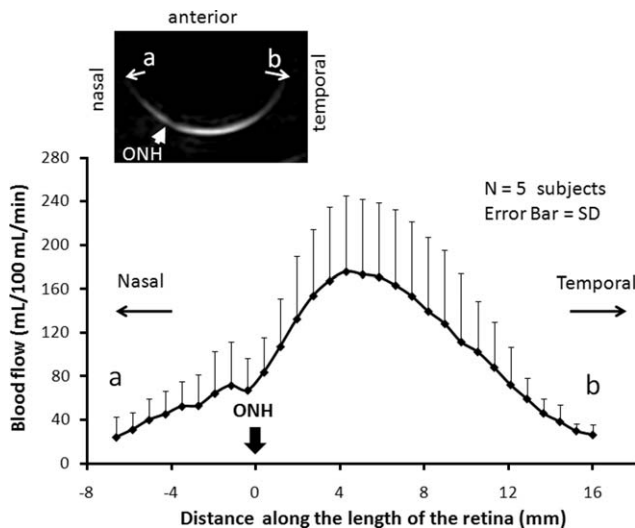


FIG. 2. Group-averaged basal BF as a function of distance from the length of the retina as shown in the inset. ONH: optic nerve head.

images from the ROI of the posterior retina, and a quantitative BF map under basal condition from one subject. The perfusion signal ΔS from the entire retina typically ranged from 15% to 25% of raw MRI images. Quantitative BF image showed excellent BF contrast, with high BF localized to the posterior retina.

BF profiles were analyzed as a function of distance from the optic nerve head (Fig. 2). BF in the retina was markedly above noise level as indicated by the negligible BF values in the vitreous and sclera on either side of the BF profile. The average SNR of the basal BF from the posterior retina was 22 ± 9 ($N = 3$ subjects). BF showed a strong spatially dependent peaking around the fovea regions and dipped slightly around the optic nerve head relative to its surrounding, and dropping significantly at the distal edges of the retina. Quantitative BF profiles were also analyzed across the thickness of the retina (from sclera to vitreous) (Fig. 3). The group-averaged BF value (peak) was 93 ± 31 mL/(100 mL min), and the group-averaged full width at half maximum (FWHM) of the blood-flow profile was 709 ± 55 μ m under basal condition.

BF percent-change correlation maps due to hypercapnic inhalation showed the BF responses highly localized to the retina (Fig. 4, two repeated trials from one subject). Quantitative BF profiles across the thickness of the retina (from sclera to vitreous) showed robust hypercapnia-evoked BF increases in the retina. Basal BF and hypercapnia-induced BF changes for individual subjects and averaged data are summarized in Fig. 5 and Table 1. Hypercapnia (5% CO₂ in air) increased BF by $12 \pm 4\%$ ($P < 0.01$) from 93 ± 31 (air) to 104 ± 35 mL/(100 mL min). The mean FWHM of the blood-flow profile was 718 ± 60 μ m under hypercapnic conditions, not statistically different from that under basal conditions ($P > 0.05$). No significant responses were detected in the lens and vitreous as expected. The rough measures of reproducibility by taking the standard deviations of multiple trials were 14.2% for basal BF and 14.5% for hypercapnic conditions (Table 1).

DISCUSSION

This study demonstrates a proof of concept that quantitative basal BF and its responses to hypercapnic challenge in unanesthetized human retina can be imaged using noninvasive MRI. A custom-designed eye surface coil improves SNR in the posterior retina compared to standard head volume coils, pseudocontinuous arterial spin-labeling technique improves sensitivity for BF measurement, and high turbo-spin echo acquisition yields images free of susceptibility artifacts. Synchronized eye blink minimizes eye movement, and synchronized respiration reduces physiological fluctuation, respectively. ASL blood-flow MRI is: (i) noninvasive, (ii) depth-resolved and unhindered by media opacity, (iii) quantitative, allowing comparison across subjects, and (iv) sensitive, capable of detecting changes associated with mild hypercapnic inhalation. MRI has the potential to provide a valuable tool to study how BF is regulated in the normal retina (i.e., neurovascular coupling), and how retinal diseases may affect basal BF and blood-flow regulation in vivo. Although improvement in spatial resolution is needed, this study sets the stage for further exploration of BF MRI of the human retina in normal and diseased states.

Potential Issues

There are four potential confounds in imaging BF of the human retina using MRI, namely, spatiotemporal resolution, susceptibility artifacts, movement artifacts, and assumptions in the BF calculation.

Spatiotemporal Resolution

The unique advantages of BF MRI include depth resolution, images unhindered by media opacity, and a large field of view, compared to many optical imaging techniques. Moreover, in contrast to most imaging approaches, MRI measures tissue perfusion of labeled water in the whole tissue within a voxel without the need to resolve individual vessels. The key disadvantages of BF MRI include poorer spatial and temporal resolution compared to optical imaging techniques. The need for synchronizing eye fixation to a target, particularly in some patients with eye diseases, may limit BF MRI application to the

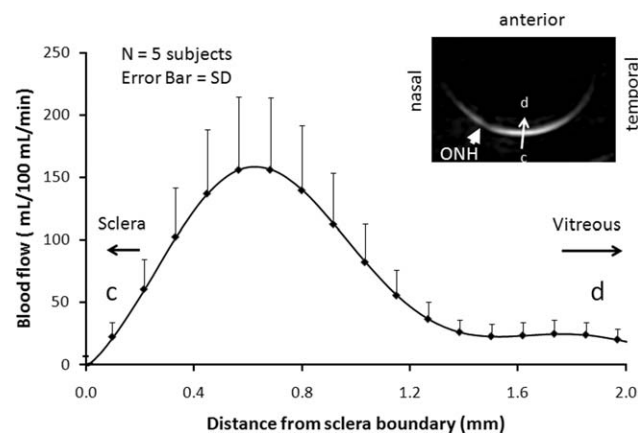


FIG. 3. Group-averaged BF profiles under air inhalation across the retinal thickness from vitreous to sclera as shown in the inset.

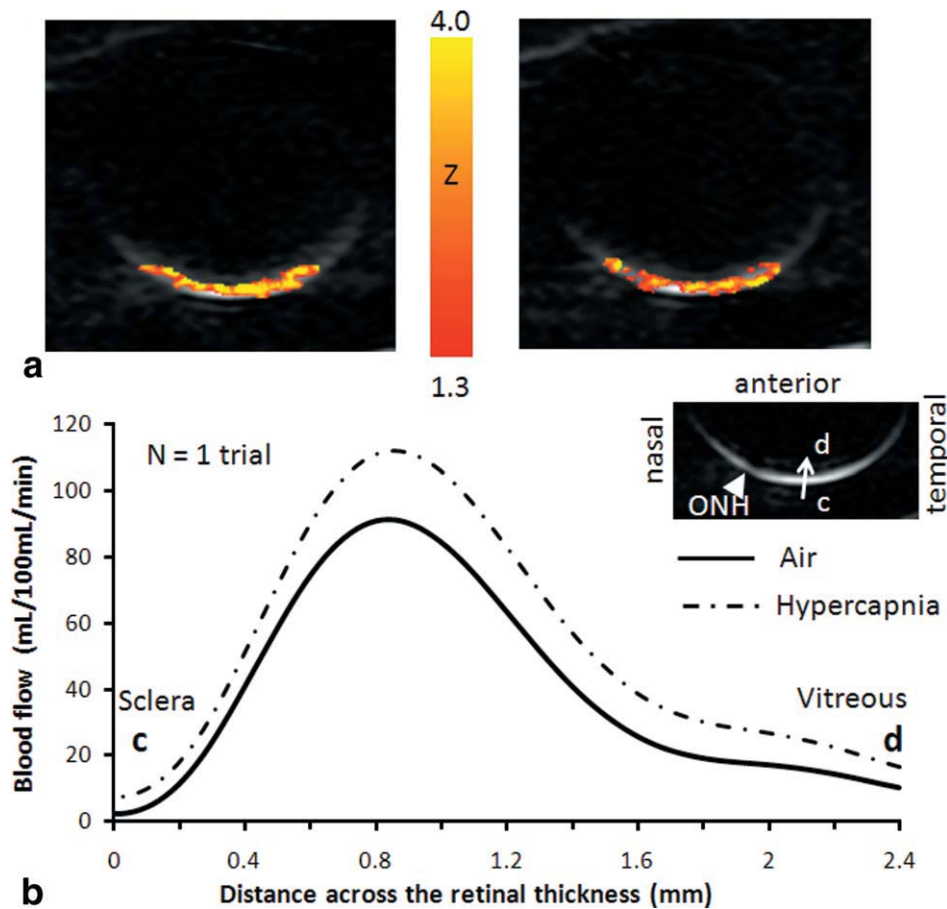


FIG. 4. (A) Hypercapnia-induced blood-flow activation maps from two repeated trials from the same subject. Color maps are overlaid on the blood flow images. Color bar indicates Z scores. (B) BF profiles under air (solid line curve) and hypercapnic inhalation (dotted line curve) across the retinal thickness from vitreous to sclera as shown in the inset.

retina. PVE was significant and would likely result in underestimated BF values because the vitreous and sclera on either side of the retina had no significant BF. With the adult human eye of 25 mm in diameter, a central imaging slice of 6 mm yielded a significant PVE from the retinal curvature (61% of total retinal thickness including the choroid, assuming a spherical eyeball). Although the spatial resolution of 500 μm was high compared to typical brain studies, it yielded about one pixel across the human retinal thickness, which is 600 μm including the choroid (27) (see discussion below). The current resolution precludes imaging different BF layers within the retina. Future studies will need to improve spatial resolution and sensitivity to differentiate BF between the retinal and choroidal vasculatures.

Potential Susceptibility Artifacts

The eye is located close to air-tissue and bone-tissue interfaces and thus has severe magnetic field inhomogeneity. Single-shot and multishot echo-planar imaging of the retina were explored but unfortunately yielded severe susceptibility-induced image distortion and signal drop off (data not shown). TSE acquisition was thus implemented to achieve high spatial resolution MRI free of susceptibility artifacts. Specific absorption rate was not an issue with the pCASL TSE acquisition as the protocol was essentially identical to typical human brain BF measurements and was confirmed by the scanner specific absorption rate safety monitor.

Potential Movement Artifacts

High-resolution BF imaging of the retina may also be more susceptible to hardware drift and eye movement artifacts because: (i) high-resolution imaging pulse sequence is more demanding on gradient performance of the scanner, which could lead to temperature-induced frequency and signal drift. We confirmed with our imaging protocols on phantoms that there was no significant drift due to hardware over half an hour of continuous scanning of the BF MRI protocol. (ii) The thin retina is bounded by the sclera and the vitreous which have very different signal intensities than the retina. Misregistration of the time-series

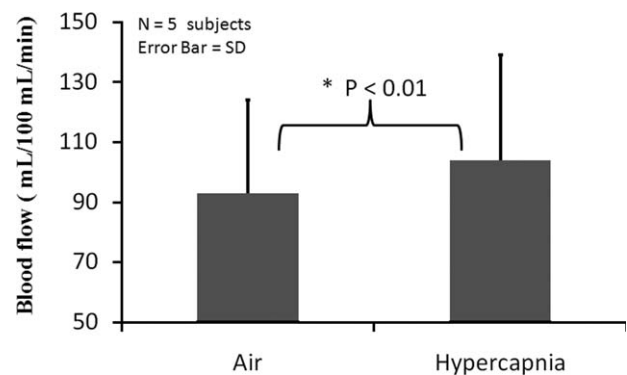


FIG. 5. Group-averaged blood flow under air and hypercapnic (5% CO_2) inhalation. Error bars are standard deviations for $N = 5$ subjects. $P < 0.01$.

Table 1

Blood Flow (mL/[100 mL min], mean \pm SD) of the Human Retina During Air and Hypercapnia (5% CO₂ in air) Inhalation from Individual Subjects Obtained from Profile Analysis of the Peak Values for Each Trial Individually

Subject ID	Gender	Age	Sessions	Trials	Air	Hypercapnia	% changes
1 ^a	Male	24	4	5	143 \pm 46 ^b	161 \pm 45	14 \pm 7 %
2	Male	35	3	5	63 \pm 9	73 \pm 12	15 \pm 5 %
3	Female	25	3	4	70 \pm 3	77 \pm 3	10 \pm 4 %
4	Male	45	1	3	98 \pm 6	113 \pm 11	16 \pm 6 %
5	Male	24	1	1	92	99	7 %
Average ^c			12	19	93 \pm 31	104 \pm 35	12 \pm 4 %*

Studies of each session were performed on different days on the same subjects. Multiple fMRI trials were performed in each session except subject #5 to assess reproducibility.

* $P < 0.01$, one-way ANOVA with correction for correlated samples.

^aStandard deviations from each subject were taken across multiple trials.

^bThis subject had a reproducible high blood flow, relative to others.

^cAverages and standard deviations were taken across all subjects ($N = 5$).

images could thus lead to significant errors. We therefore applied background suppression to null the otherwise bright vitreous signal. (iii) Finally, ASL BF MRI requires subtraction of paired images and is thus more susceptible to motion that may occur between acquisitions of the paired images. Thus, it is necessary to carefully evaluate ASL signal stability by evaluating time-loop movies and signal time courses to ensure no sudden jump or significant drift. With synchronized eye blink and respiration, movement and drift were small and residual eye movement could be corrected by image coregistration. All images were acquired in time series and coregistered if needed before signal averaging and crosscorrelation analysis.

Quantitative BF Calculation

Absolute quantification of BF is generally difficult and the commonly used MRI, positron emission tomography (PET), LDF, and microsphere techniques have strengths and limitations. The pCASL MRI technique to measure BF of the retina has the following limitations. Firstly, the BF quantification formula used in this work is based on a simplified single blood compartment model, assuming that the labeled water does not cross the capillary wall or leave the voxel between labeling and signal acquisition. Secondly, BF calculation used estimated values for the blood labeling efficiency. Further validation of these parameters will improve the accuracy of BF quantification for human retina. BF MRI of the brain has been cross-validated with PET and autoradiographic techniques. Ultimately, ASL MRI of the retina needs to be cross-validated with the microsphere technique in animal models. Improving accuracy of quantitative BF MRI remains an active area of research.

Human Retinal Thickness by BF Profile

From BF profile across the retinal thickness, the FWHM was $709 \pm 55 \mu\text{m}$ (including the choroidal vascular layer). Although this is expected to be slightly different anatomical thickness, it is informative to compare. Published thicknesses of the in vivo human neural retina (excluding the choroid) varied significantly, even within the optical coherence tomography literature— $236 \mu\text{m}$ (26) and $200\text{--}310 \mu\text{m}$ (27) around the fovea. While optical coherence tomography can resolve laminar thickness of the neural ret-

ina, measuring choroidal thickness by optical imaging techniques remains challenging. Sparsely published in vivo human choroidal thickness has been reported to be $293\text{--}307 \mu\text{m}$ by partial coherence interferometry (28) and $318\text{--}335 \mu\text{m}$ by long-wavelength optical coherence tomography (29). From these literatures, we estimated the total anatomical retinal thickness including the choroid from non-MRI measurement to be $500\text{--}650 \mu\text{m}$ (in the posterior retina) albeit there was strong spatial dependence. By comparison, the rodent retinal thickness is $267 \mu\text{m}$ including the choroid (24), and the cat retinal thickness is $358 \mu\text{m}$ including the choroid (31), suggesting a scaling of retinal thickness with eye size.

Basal BF

Basal BF of the total retina, including the choroid was $93 \pm 31 \text{ mL}/(100 \text{ mL min})$ in awake human. To our knowledge, this is the first in vivo BF measurement in the unanesthetized human retina, and there are no reports in the literature with which to compare. In animal model, basal BF of the rat retina has been reported to be $630 \pm 100 \text{ mL}/(\text{g min})$ under 1% isoflurane using cASL MRI (13,14). The differences in BF of the retina between humans and rats could arise from many factors. They include species differences, spatial resolution differences (lower spatial resolution has more PVE, which yields lower BF), and the effect of isoflurane which is a vasodilator.

By comparison, in awake human, brain gray-matter BF was $\sim 50 \text{ mL}/(100 \text{ mL min})$ (10) using the same pCASL MRI technique. In anesthetized rats, brain gray-matter BF was $90 \pm 13 \text{ mL}/(100 \text{ g min})$ (28) and $110 \pm 4 \text{ mL}/(100 \text{ g min})$ (29) under essentially identical experimental conditions (i.e., $\sim 1\%$ isoflurane) as those reported for rat retina described above. The BF retina:brain ratio was reported to be 6.3:1 in rat and 2:1 in human (this study). The smaller BF retina:brain ratio in humans compared to animals could be due to comparatively lower spatial resolution, effect of isoflurane, and/or species differences. Of note, destructive microsphere BF measurements in animal models that provided retinal and choroid BF values, reported that retinal BF was similar to cerebral BF in the gray matter whereas choroidal BF was about 6 to 10 times higher than cerebral BF in rats (30) and monkeys (31).

BF MRI provides large field of view, in contrast to optical imaging techniques which have limited field of view constrained by illumination angle. BF was observed to drop significantly at the distal edges of the retina, consistent with those reported previously in animal models (13,14). This is expected because the vascular density is highest around the optic nerve head but drops distally. BF showed a strong spatial dependence, peaking around the foveal regions. This appears to contradict the notion that the fovea is free of retinal vessels and thus should have lower BF compared to surrounding region. A possible explanation is that the current spatial resolution precludes the fine resolution of the fovea, and MRI BF signal of the macular ROI at current resolution is dominated by choroidal BF.

BF dipped slightly around the optic nerve head relative to its immediately surrounding as detected by MRI. This is consistent with the optic nerve head anatomy. It is however surprising that BF in the optic nerve head ROI is less than the foveal ROI because optic nerve head is densely populated by large arteries and veins. It is possible that the ASL technique is generally less sensitive to large water-impermeable vessels and more sensitive to smaller vessels (such as arterioles, capillaries and venules) (32,33) due to a longer postlabeling used allowing labeled spins to leave large arteries and move into smaller vessels, and the labeled spins lose substantial contrast (with a time constant T_1 of ~ 1.5 sec) by the time they reach large draining veins. Being more sensitive to smaller vessels (34) is advantageous because it reflects local tissue perfusion and is more spatially specific to the sites of increased neuronal activities.

BF Changes

Hypercapnic (5% CO₂ in air) inhalation increased BF of the unanesthetized human retina by $12 \pm 4\%$. In isoflurane-anesthetized rats, hypercapnic inhalation increased BF by $16 \pm 6\%$ using BF MRI (13). BF MRI of animal and human retinas showed consistent positive BF increases during hypercapnic inhalation. While there is evidence that hypercapnia elicits vasodilation in both retinal and choroid blood vessels using LDF and microsphere techniques (35–38), the literature are sparse and inconsistent. Inhalation of 10% CO₂ in air showed no significant vasodilation in the retinal vessels (39). Inhalation of carbogen (95% O₂ + 5% CO₂) increased choroid BF by $12.5 \pm 11.7\%$ with large intersubject variations (40). Pulsatile ocular BF tonography also reported significant choroidal BF increases (41).

By comparison, in the rat brain, hypercapnic (5% CO₂ in air) inhalation-increased cerebral BF varied over a wide range in anesthetized rats, ca., 25% (42) and 52% (29). Similar hypercapnia-induced changes in cerebral BF in awake humans have also been reported in the literature. Hypercapnia-induced BF increase in the retina is smaller than that in the brain, which could be due to PVE or the unique responses of the retina.

Finally, caution must be exercised when comparing BF measurements among LDF, microsphere, and MRI techniques because they have different signal sources. Microsphere values may be susceptible to postmortem

artifacts and may vary depending on microsphere size and concentration (43). LDF typically measures a single point source within the probe sensitivity whereas BF in the retina has a spatial dependence. Retinal BF measured using LDF is limited to the optic nerve head and could be contaminated by choroidal BF because LDF has ambiguous depth resolution. Choroid BF by LDF is limited to the macular region where retinal vessels are absent. BF MRI offers a large field of view and not depth limited, but takes significantly longer to acquire. BF MRI may have the unique potential to image layer-specific, quantitative BF in human retina if higher spatial resolution can be achieved. In addition to BF, MRI also provides anatomical, oxygen tension and functional data. MRI has recently been applied to investigate structures of the retina (19,44), changes in tissue oxygenation using blood oxygenation level-dependent (BOLD) functional MRI associated with physiologic (19) and visual (45,46) stimulation in animal models. Changes in layer thickness and BOLD functional MRI responses to physiologic challenges in an animal model of retinitis pigmentosa in which the photoreceptors progressively degenerate have also been reported (19). Translating these approaches to image the human retina may have important applications.

CONCLUSIONS

This study reports our initial experience on imaging basal BF and hypercapnia-induced blood-flow changes in the retina of unanesthetized humans. Future studies will need to improve sensitivity and spatiotemporal resolution, incorporate three-dimensional BF and other (e.g., BOLD and anatomical) MRI methods, and apply multimodal MRI approach to study retinal diseases. With improvement in spatiotemporal resolution and sensitivity, MRI has the potential to provide unique information, with depth resolution, on how BF is regulated and how retinal diseases may affect BF and the neural tissues they subserve, as well as the ability to serve as an objective biomarker for staging disease, monitoring of therapeutic intervention, and testing novel therapeutic strategy. This approach could open up new avenues for retinal research and complement existing retinal imaging techniques.

ACKNOWLEDGMENTS

Qi Peng and Yi Zhang contributed equally to this work. This work was supported by a Clinical Translational Science Award Pilot Grant (to TQD) and a Translational Technology Resource Grant (to QP) (parent grant UL1RR025767). TQD received supports from the NIH/NEI (R01 EY014211 and EY018855), and the VISN7 Career Development Award and MERIT from the Department of Veterans Affairs.

REFERENCES

1. Raichle ME. Circulatory and metabolic correlates of brain function in normal humans. In: Plum F, editor. Handbook of physiology—the nervous system, vol. V: higher functions of the brain. Bethesda: American Physiological Society; 1987. pp 643–674.
2. Pemp B, Schmetterer L. Ocular blood flow in diabetes and age-related macular degeneration. *Can J Ophthalmol* 2008;43:295–301.

3. Pournaras CJ, Rungger-Brandle E, Riva CE, Hardarson SH, Stefansson E. Regulation of retinal blood flow in health and disease. *Prog Retin Eye Res* 2008;27:284–330.
4. Preussner PR, Richard G, Darrelmann O, Weber J, Kreissig I. Quantitative measurement of retinal blood flow in human beings by application of digital image-processing methods to television fluorescein angiograms. *Graefes Arch Clin Exp Ophthalmol* 1983;221:110–112.
5. Guyer DR, Yannuzzi LA, Slakter JS, Sorenson JA, Orlock S. The status of indocyanine-green videoangiography. *Cur Opin Ophthalmol* 1993;4:3–6.
6. Formaz F, Riva CE, Geiser M. Diffuse luminance flicker increases retinal vessel diameter in human. *Curr Eye Res* 1997;16:1252–1257.
7. Cheng H, Duong TQ. Simplified laser-speckle-imaging analysis method and its application to retinal blood flow imaging. *Opt Lett* 2007;32:2188–2190.
8. Cheng H, Yan Y, Duong TQ. Temporal statistical analysis of laser speckle image and its application to retinal blood-flow imaging. *Optics Express* 2008;16:10214–10219.
9. Ostergaard L, Sorensen AG, Kwong KK, Weisskoff RM, Gyldensted C, Rosen BR. High resolution measurement of cerebral blood flow using intravascular tracer bolus passages. Part II. Experimental comparison and preliminary results. *Magn Reson Med* 1996;36:726–736.
10. Detre JA, Leigh JS, Williams DS, Koretsky AP. Perfusion imaging. *Magn Reson Med* 1992;23:37–45.
11. Calamante F, Thomas DL, Pell GS, Wiersma J, Turner R. Measuring cerebral blood flow using magnetic resonance imaging techniques. *J Cereb Blood Flow Metab* 1999;19:701–735.
12. Williams DS, Detre JA, Leigh JS, Koretsky AP. Magnetic resonance imaging of perfusion using spin inversion of arterial water. *Proc Natl Acad Sci USA* 1992;89:212–216.
13. Li Y, Cheng H, Duong TQ. Blood-flow magnetic resonance imaging of the retina. *Neuroimage* 2008;39:1744–1751.
14. Li Y, Cheng H, Shen Q, Kim M, Thule PM, Olson DE, Pardue MT, Duong TQ. Blood-flow magnetic resonance imaging of retinal degeneration. *Invest Ophthalmol Vis Sci* 2009;50:1824–1830.
15. Alsop DC, Maldjian JA, Detre JA. In vivo MR perfusion imaging of the human retina. In: *Proc Int Soc Magn Reson Med*, Denver, CO; 2000. p 162.
16. Dai W, Garcia D, de Bazelaire C, Alsop DC. Continuous flow-driven inversion for arterial spin labeling using pulsed radio frequency and gradient fields. *Magn Reson Med* 2008;60:1488–1497.
17. Mani S, Pauly J, Conolly S, Meyer C, Nishimura D. Background suppression with multiple inversion recovery nulling: applications to projective angiography. *Magn Reson Med* 1997;37:898–905.
18. Buecker A, Adam G, Neuerburg JM, Glowinski A, van Vaals JJ, Guenther RW. MR-guided biopsy using a T2-weighted single-shot zoom imaging sequence (Local Look technique). *J Magn Reson Imaging* 1998;8:955–959.
19. Cheng H, Nair G, Walker TA, Kim MK, Pardue MT, Thule PM, Olson DE, Duong TQ. Structural and functional MRI reveals multiple retinal layers. *Proc Natl Acad Sci USA* 2006;103:17525–17530.
20. Chalela JA, Alsop DC, Gonzalez-Atavales JB, Maldjian JA, Kasner SE, Detre JA. Magnetic resonance perfusion imaging in acute ischemic stroke using continuous arterial spin labeling. *Stroke* 2000;31:680–687.
21. Herscovitch P, Raichle ME. What is the correct value for the brain-blood partition coefficient for water? *J Cereb Blood Flow Metab* 1985;5:65–69.
22. Lu H, Clingman C, Golay X, van Zijl PC. Determining the longitudinal relaxation time (T1) of blood at 3.0 Tesla. *Magn Reson Med* 2004;52:679–682.
23. Stanisz GJ, Odobina EE, Pun J, Escaravage M, Graham SJ, Bronskill MJ, Henkelman RM. T1, T2 relaxation and magnetization transfer in tissue at 3T. *Magn Reson Med* 2005;54:507–512.
24. Wu WC, Fernandez-Seara M, Detre JA, Wehrli FW, Wang J. A theoretical and experimental investigation of the tagging efficiency of pseudocontinuous arterial spin labeling. *Magn Reson Med* 2007;58:1020–1027.
25. Garcia DM, Duhamel G, Alsop DC. Efficiency of inversion pulses for background suppressed arterial spin labeling. *Magn Reson Med* 2005;54:366–372.
26. Smith SM, Jenkinson M, Woolrich MW, Beckmann CF, Behrens TE, Johansen-Berg H, Bannister PR, De Luca M, Drobnjak I, Flitney DE, Niazky RK, Saunders J, Vickers J, Zhang Y, De Stefano N, Brady JM, Matthews PM. Advances in functional and structural MR image analysis and implementation as FSL. *Neuroimage* 2004;23 (Suppl 1):S208–219.
27. Peng Q, Zhang Y, Duong TQ. MRI laminar resolution of the human retina. In: *Proc Int Soc Magn Reson Med*, Stockholm, Sweden;2010. p 688.
28. Liu ZM, Schmidt KF, Sicard KM, Duong TQ. Imaging oxygen consumption in forepaw somatosensory stimulation in rats under isoflurane anesthesia. *Magn Reson Med* 2004;52:277–285.
29. Sicard KM, Duong TQ. Effects of hypoxia, hyperoxia and hypercapnia on baseline and stimulus-evoked BOLD, CBF and CMRO2 in spontaneously breathing animals. *NeuroImage* 2005;25:850–858.
30. Wang L, Fortune B, Cull G, McElwain KM, Cioffi GA. Microspheres method for ocular blood flow measurement in rats: size and dose optimization. *Exp Eye Res* 2007;84:108–117.
31. Alm A, Bill A. Ocular and optic nerve blood flow at normal and increased intraocular pressures in monkeys (*Macaca irus*): a study with radioactively labelled microspheres including flow determinations in brain and some other tissues. *Exp Eye Res* 1973;15:15–29.
32. Duong TQ, Kim D-S, Ugurbil K, Kim S-G. Localized blood flow response at sub-millimeter columnar resolution. *Proc Natl Acad Sci USA* 2001;98:10904–10909.
33. Calamante F, Gadian DG, Connelly A. Quantification of perfusion using bolus tracking magnetic resonance imaging in stroke: assumptions, limitations, and potential implications for clinical use. *Stroke* 2002;33:1146–1151.
34. Duong TQ, Kim D-S, Ugurbil K, Kim S-G. Localized blood flow response at sub-millimeter columnar resolution. *Proc Natl Acad Sci USA* 2001;98:10904–10909.
35. Alm A, Bill A. The oxygen supply to the retina. II. Effects of high intraocular pressure and of increased arterial carbon dioxide tension on uveal and retinal blood flow in cats. *Acta Physiol Scand* 1972;84:306–319.
36. Alm A, Bill A. The oxygen supply to the retina I. Effects of changes in intraocular and arterial blood pressures, and in arterial pO₂ and pCO₂ on the oxygen tension in the vitreous body of the cat. *Acta Physiol Scand* 1972;84:261–274.
37. Friedman E, Chandra SR. Choroidal blood flow. III. Effects of oxygen and carbon dioxide. *Arch Ophthalmol* 1972;87:70–71.
38. Cioffi GA, Granstam E, Alm A. Ocular circulation. In: Kaufman PL, Alm A, editors. *Adler's physiology of the eye clinical application*. St. Louis: Mosby; 2003. pp 747–784.
39. Frayser R, Hickam JB. Retinal vascular response to breathing increased carbon dioxide and oxygen concentrations. *Invest Ophthalmol Vis Sci* 1964;3:427–431.
40. Geiser MH, Riva CE, GDormer GT, Diermann U, Luksch A, Schmetterer L. Response of choroidal blood flow in the foveal region to peroxia and hyperoxia-hypercapnia. *Current Eye Res* 2000;21:669–676.
41. Kergoat H, Faucher C. Effects of oxygen and carbogen breathing on choroidal hemodynamics in humans. *Invest Ophthalmol Vis Sci* 1999;40:2906–2911.
42. Sicard K, Shen Q, Brevard ME, Sullivan R, Ferris CF, King JA, Duong TQ. Regional cerebral blood flow and BOLD responses in conscious and anesthetized rats under basal and hypercapnic conditions: implications for functional MRI studies. *J Cereb Blood Flow Metab* 2003;23:472–481.
43. Kuznetsova LV, Tomasek N, Sigurdsson GH, Banic A, Erni D, Wheatley AM. Dissociation between volume blood flow and laser-Doppler signal from rat muscle during changes in vascular tone. *Am J Physiol* 1998;274:H1248–1254.
44. Shen Q, Cheng H, Chang TF, Nair G, Shonat RD, Pardue MT, Toi VV, Duong TQ. Magnetic resonance imaging of anatomical and vascular layers of the cat retina. *J Magn Reson Imaging* 2006;23:465–472.
45. Duong TQ, Ngan S-C, Ugurbil K, Kim S-G. Functional magnetic resonance imaging of the retina. *Invest Ophthalmol Vis Sci* 2002;43:1176–1181.
46. De La Garza B, Li G, Muir E, Shih YY, Duong TQ. BOLD fMRI of Visual Stimulation in the Rat Retina at 11.7 Tesla. *NMR Biomed*, 2010. Online Dec 3, 2010. PMID 21132673.